ADVANCED ENERGY MATERIALS

Supporting Information

for *Adv. Energy Mater.,* DOI: 10.1002/aenm.202003336

Enabling 6C Fast Charging of Li-Ion Batteries with Graphite/ Hard Carbon Hybrid Anodes

*Kuan-Hung Chen, Vishwas Goel, Min Ji Namkoong, Markus Wied, Simon Müller, Vanessa Wood, Jeff Sakamoto, Katsuyo Thornton, and Neil P. Dasgupta**

Supporting Information

Enabling 6C Fast Charging of Li-ion Batteries with Graphite/Hard Carbon Hybrid Anodes

*Kuan-Hung Chen, Vishwas Goel, Min Ji Namkoong, Markus Wied, Simon Müller, Vanessa Wood, Jeff Sakamoto, Katsuyo Thornton, Neil P. Dasgupta**

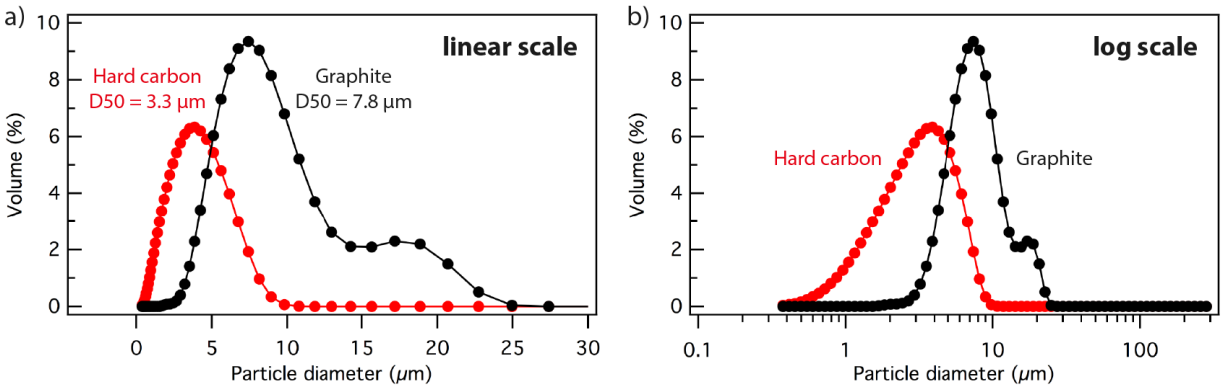

Figure S1. Particle size distribution plot for the graphite and hard carbon used in this work. The x-axis is plotted in both (a) linear scale and (b) log scale. The measured D50 value is 3.3 µm for the hard carbon and 7.8 µm for the graphite.

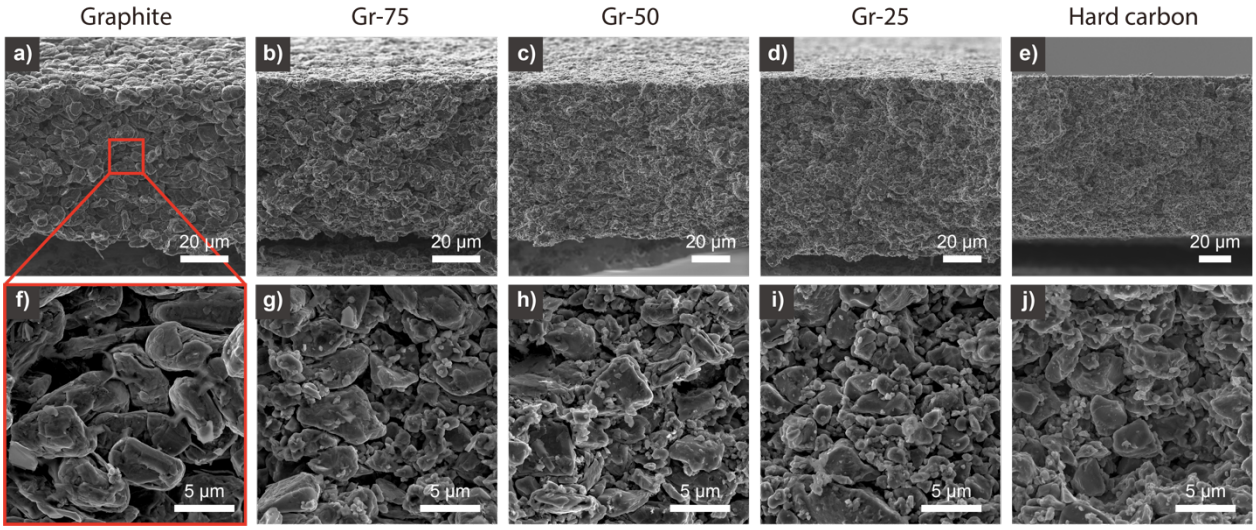

Figure S2. Cross-sectional SEM images of the graphite, Gr-75, Gr-50, Gr-25, and hard carbon electrodes.

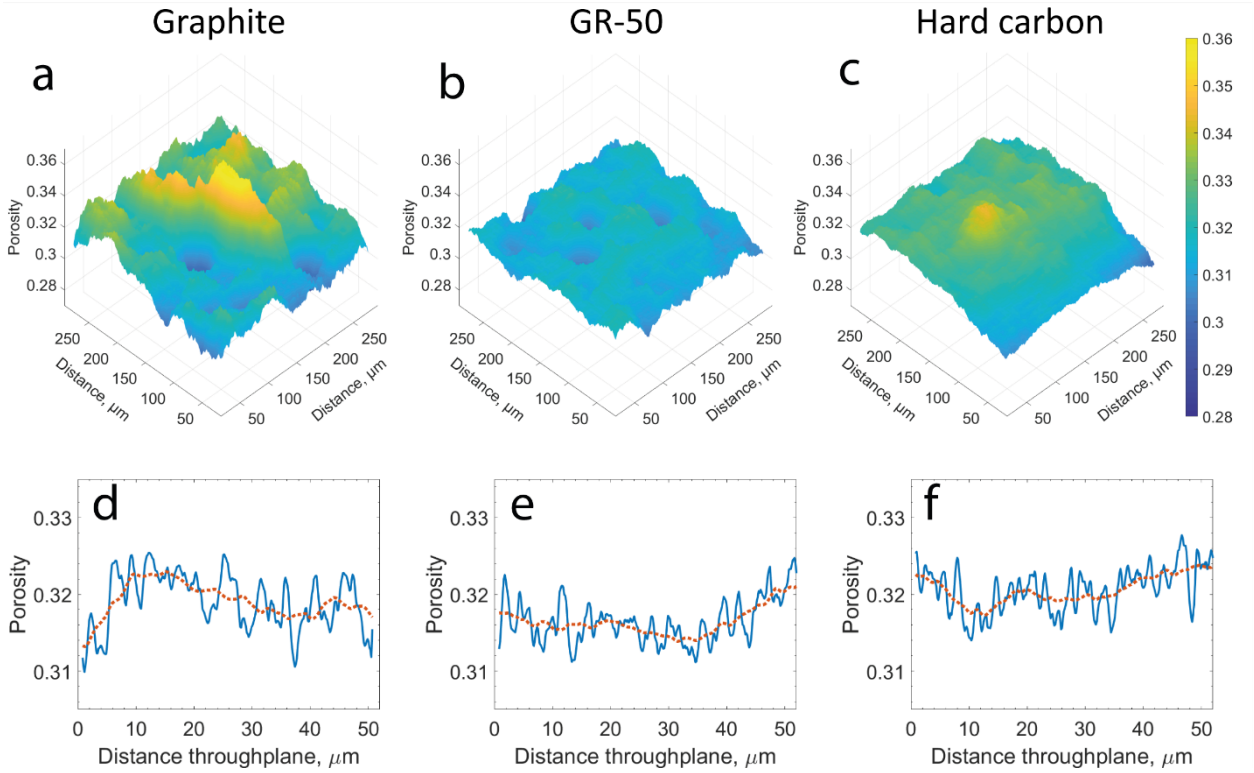

Figure S3. Porosity maps of the (a) graphite, (b) Gr-50, and (c) hard carbon electrodes obtained by calculating the porosity for each column of voxels over the through-plane. The average porosity over the in-plane direction is also calculated and plotted for the (d) graphite, (e) Gr-50, and (f) hard carbon electrodes.

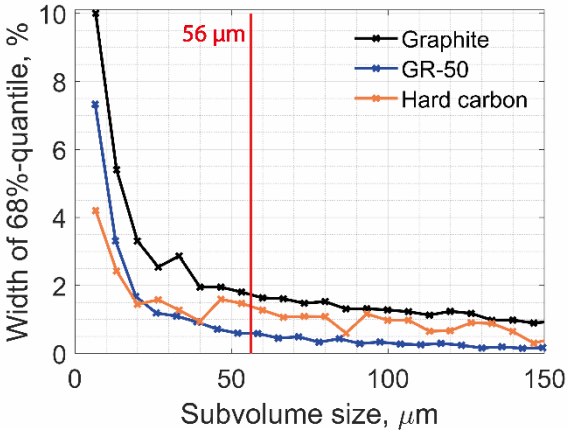

Figure S4. Scale-space analysis showing the width of 68%-quantile of the porosity distribution vs. the sub-volume size for the graphite (black), Gr-50 (blue), and hard carbon (orange) electrodes. For each sub-volume size, porosity of 100 randomly placed cubes (with the corresponding edge length) was calculated. For the tomographic analysis in this study, a sub-volume size of 56 µm is chosen.

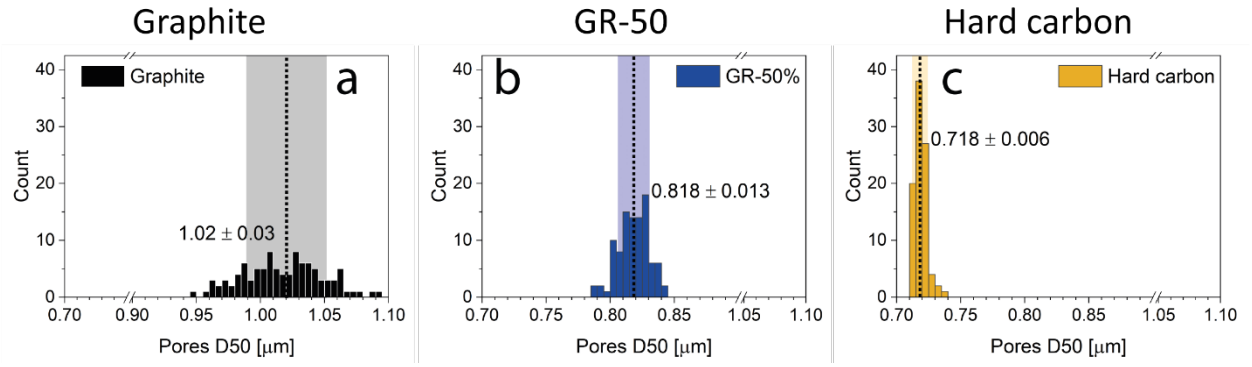

Figure S5. Average pore size distribution of the (a) graphite, (b) Gr-50, and (c) hard carbon electrodes. The dashed lines show the average values and the shaded areas show the standard deviations.

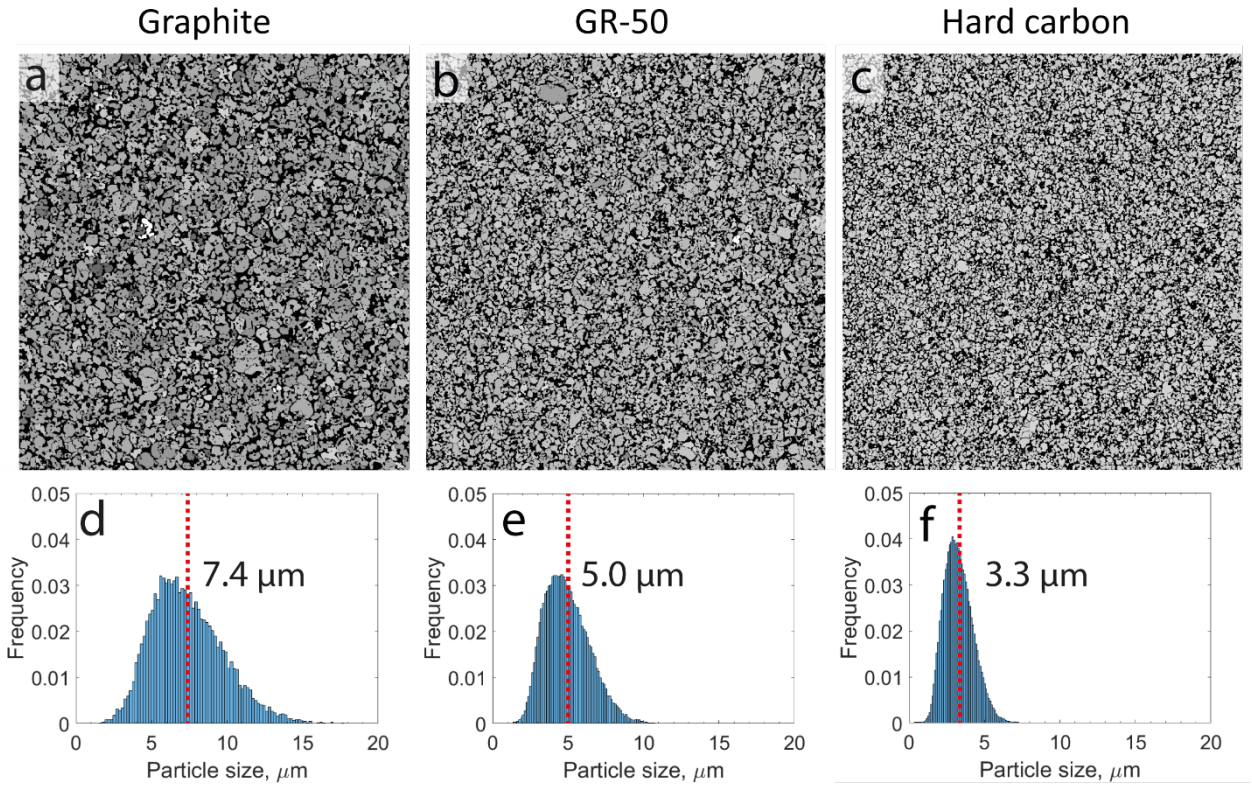

Figure S6. A single exemplary image slice of the 3-D particle segmentation using the watershed algorithm[1] for the (a) graphite, (b) Gr-50, and (c) hard carbon electrodes. Normalized histograms of the volume equivalent particle diameters are calculated for the (d) graphite, (e) Gr-50, and (f) hard carbon electrodes. The average volume equivalent particle diameters are indicated with dashed red lines.

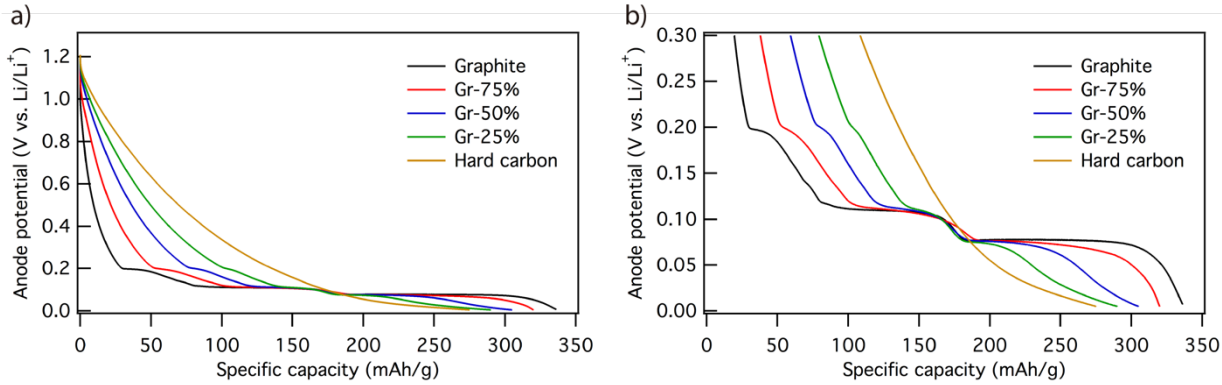

Figure S7. Three-electrode measurements showing the anode potential (with respect to a Li metal reference) vs. specific capacity (mAh/g) plots for graphite, Gr-75, Gr-50, Gr-25, and hard carbon during lithiation at a C/10 rate.

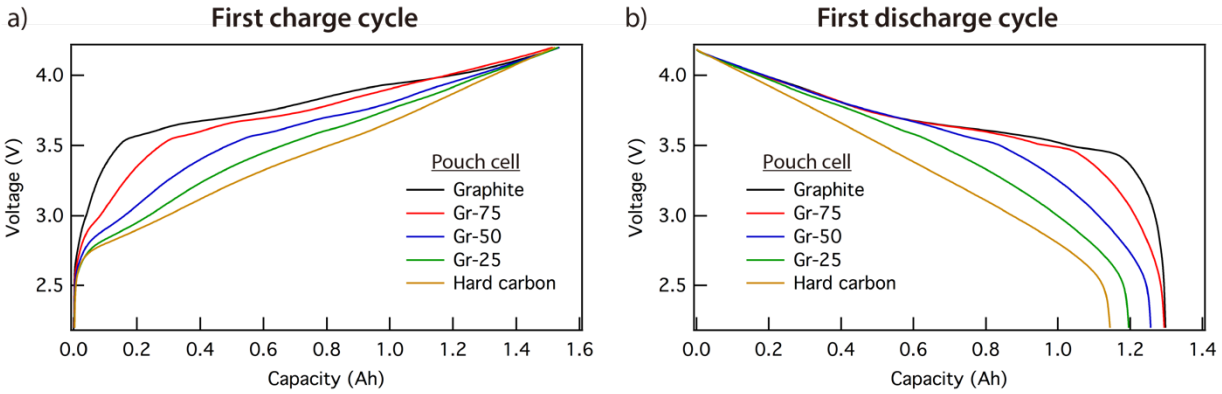

Figure S8. Voltage profiles of the graphite, Gr-75, Gr-50, Gr-25, and hard carbon pouch cells during the (a) first charge cycle and (b) first discharge cycle.

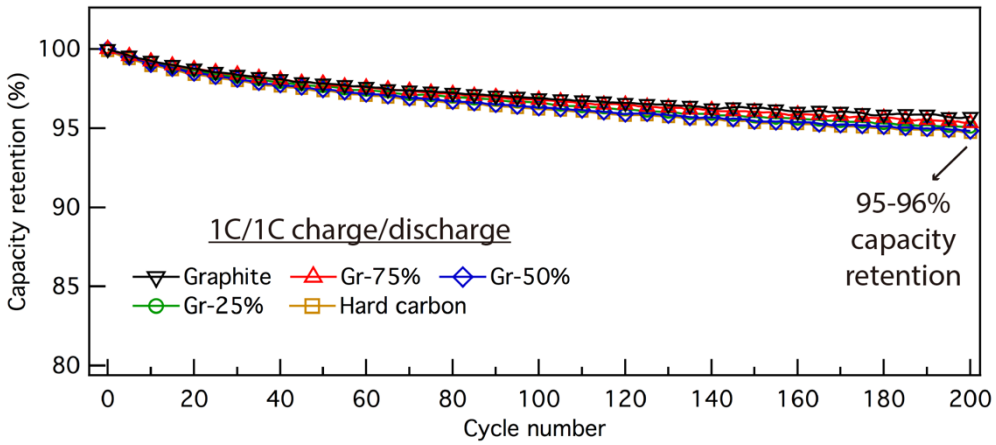

Figure S9. Normalized capacity vs. cycle number plot showing the capacity retention of all 5 types of pouch cells during 1C/1C charge/discharge cycling test. Cells were cycled between 2.7-4.2 V at 1C rate without CV hold.

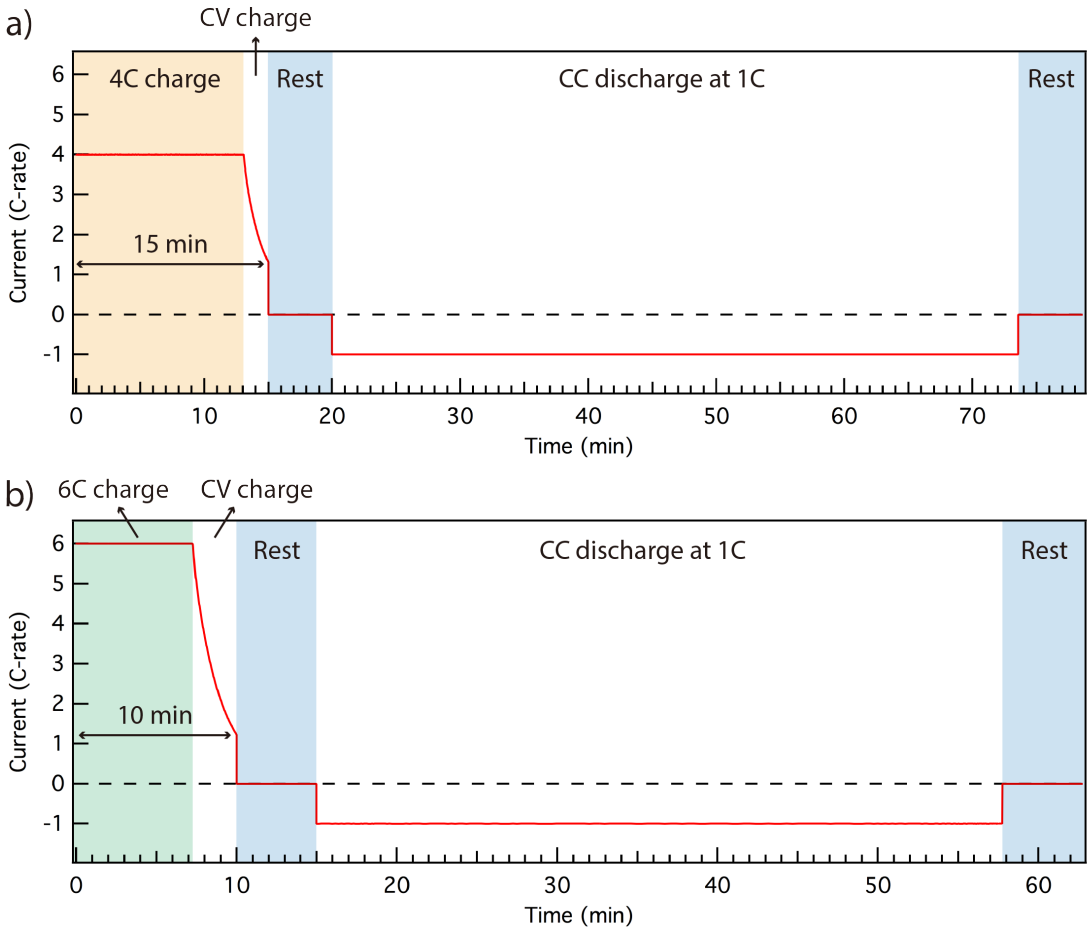

Figure S10. Cycling protocols for evaluating fast-charge capability at (a) 4C charge rate with 15-min total charging time and (b) 6C charge rate with 10-min total charging time. The discharge rate was fixed at 1C without CV hold throughout the cycling test.

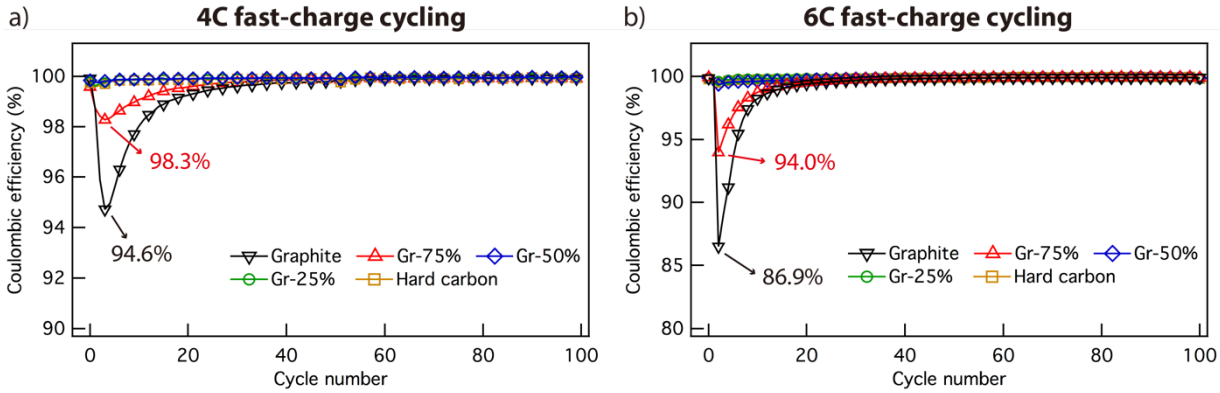

Figure S11. Coulombic efficiency vs. cycle number plots under (a) 4C and (b) 6C fast-charge conditions for the graphite, Gr-75, Gr-50, Gr-25, and hard carbon pouch cells.

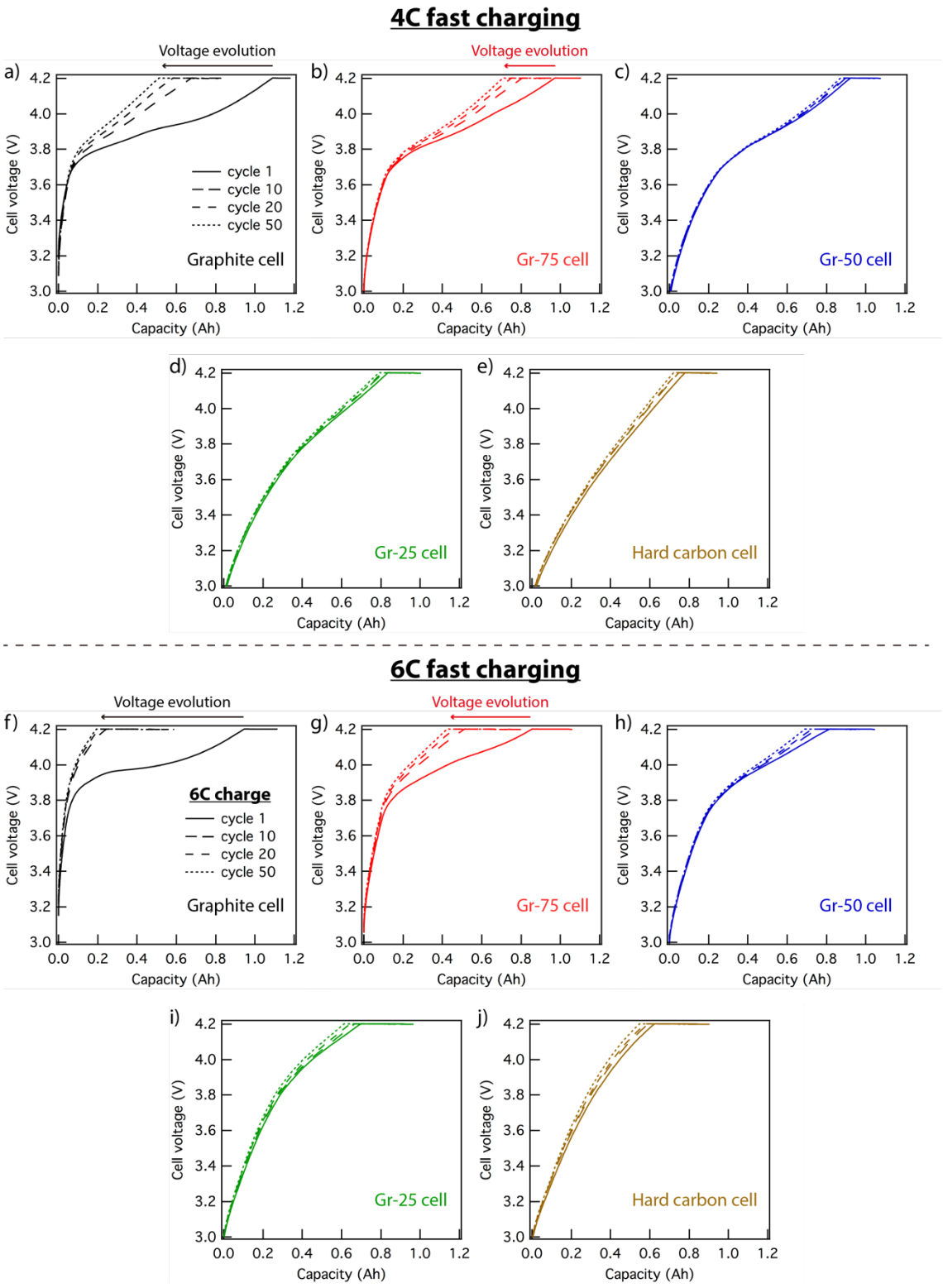

Figure S12. Cycle-to-cycle evolution of voltage traces occurring during 4C (15-min) and 6C (10-min) fast-charge cycling for the graphite, Gr-75, Gr-50, Gr-25, and hard carbon pouch cells.

	Graphite	Gr-75	Gr-50	Gr-25	Hard carbon
Cu foil thickness (µm)	10 µm				
Anode loading (mg/cm²)	9.42	9.69	10.29	10.78	11.24
Anode porosity (%)	31%	30%	32%	31%	31%
Separator thickness (µm)	12 µm				
Separator porosity (%)	47%				
Cathode loading (mg/cm²)	16.58 mg/cm²				
Cathode porosity (%)	34%				
Al foil thickness (µm)	15 µm				
Stack mass (mg/cm²)	38.98	39.46	40.9	41.45	42.37
Total area (cm²)	557.52 cm²				
Discharge energy (Wh)	4.4	4.31	4.11	3.72	3.35
Stack specific energy (Wh/kg)	202.4	195.9	180.2	161.0	141.8

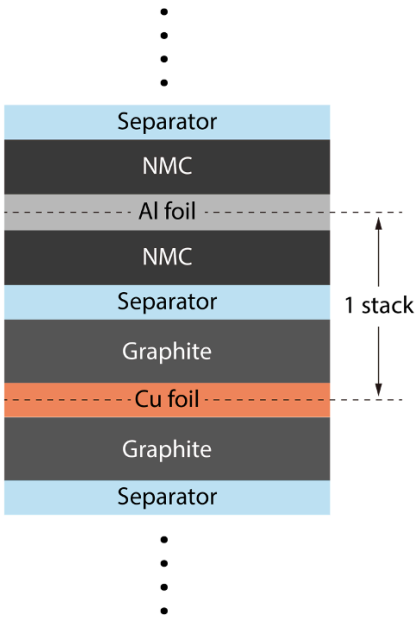

Figure S13. Stack definition and stack specific energy information for the graphite, Gr-75, Gr-50, Gr-25, and hard carbon pouch cells.

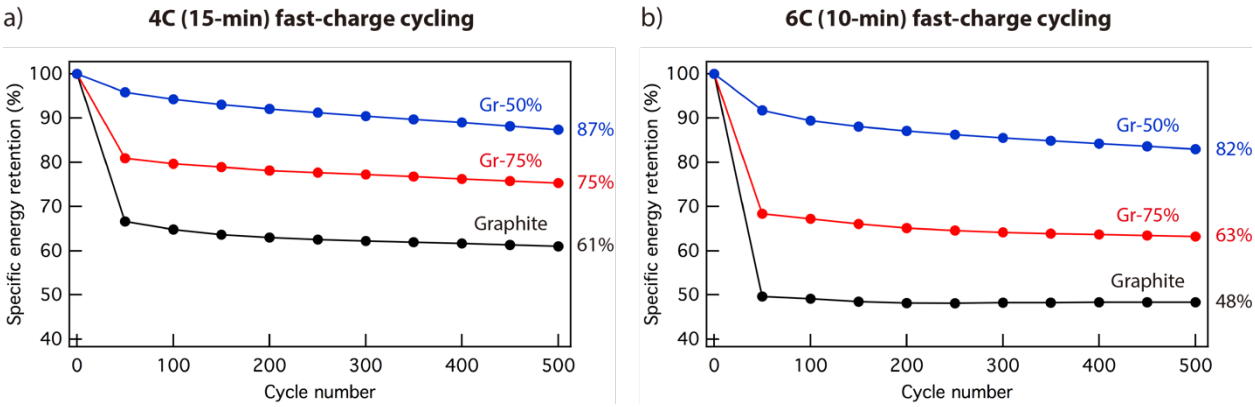

Figure S14. Specific energy retention vs. cycle number plots for the graphite, Gr-75, and Gr-50 cells during long-term (a) 4C and (b) 6C fast-charge cycling.

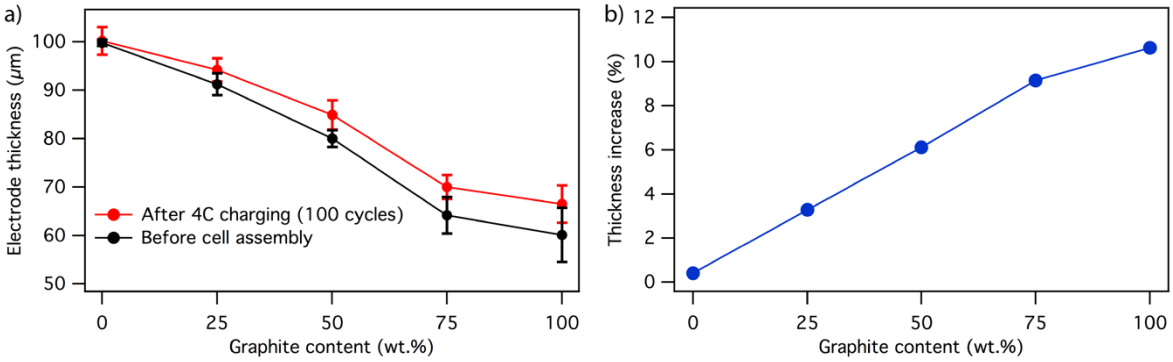

Figure S15. (a) Single-side electrode thickness and (b) percentage of thickness increase as a function of graphite content in the hybrid anodes. Only the thickness of the active material layer was measured, not the Li plating layer on the anode surface.

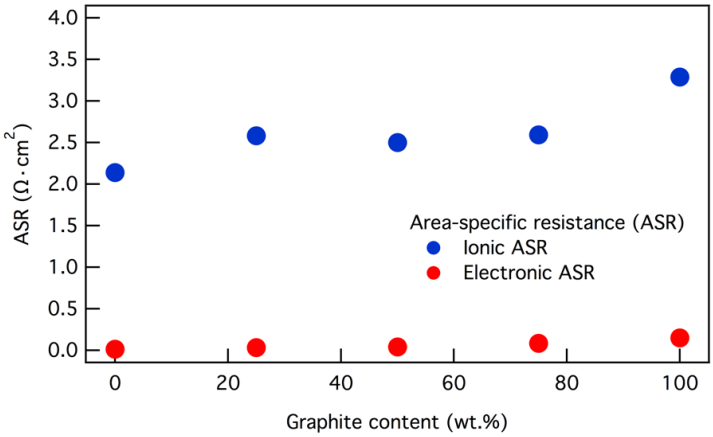

Figure S16. Ionic and electronic area-specific resistance values for the 5 hybrid anodes.

Table ST1. Effective Li-ion diffusion coefficients measured using electrochemical impedance spectroscopy.[2–4]

	Hard carbon	Gr-25	Gr-50	Gr-75	Graphite
Effective Li-ion diffusivity (m^2/s)	3.6-4.1 x 10^{-11}	2.8-3.1 x 10^{-11}	2.4-2.6 x 10^{-11}	1.4-1.5 x 10^{-11}	0.8-0.9 x 10^{-11}

Electrochemical modeling

Model equations

The model equations developed by Doyle et al.[5] based on the porous electrode theory (PET) were used to simulate the electrochemical behavior of our cells. Table ST2 contains the glossary of all the variables and symbols used in the equations. We modified the term for the reaction current per unit electrode volume given in Ref 5 to account for the presence of multiple active materials.[5] We denote the total reaction current per unit volume by R_v, which is equal to $F\sum_n a_{p,\psi}^n J_\psi^n$.

The model equations, along with the boundary conditions, are listed below. ψ indicates the domain where it is valid (see Table ST2).

$$\varepsilon_\psi \frac{\partial c_{e,\psi}}{\partial t} = \frac{\partial}{\partial z}\cdot\left(D_{eff,\psi}\,\frac{\partial c_{e,\psi}}{\partial z}\right) + \left(1-t_{+,\psi}^0\right)\frac{R_v}{F} \;-\; \frac{i_{e,\psi}}{F}\cdot\frac{\partial t_{+,\psi}^0}{\partial z} \tag{1}$$

$$i_{e,\psi} = -\,\kappa_{eff,\psi}\frac{\partial \phi_{e,\psi}}{\partial z} + \frac{2RT}{F}\kappa_{eff,\psi}\left(1+\frac{\partial\, ln\left(f_{\pm,\psi}\right)}{\partial\, ln\left(c_{e,\,\psi}\right)}\right)\left(1-t_{+,\psi}^0\right)\frac{\partial\, ln\, c_{e,\psi}}{\partial z} \tag{2a}$$

$$\frac{\partial i_{e,\psi}}{\partial z} = R_v \tag{2b}$$

$$\frac{\partial c_{p,\psi}^n}{\partial t} = \frac{1}{(r^n)^2}\frac{\partial}{\partial r^n}\left(D_{p,\psi}^n (r^n)^2\frac{\partial c_{p,\psi}^n}{\partial r^n}\right) \tag{3}$$

$$\frac{\partial}{\partial z}\cdot\left(\sigma_{eff,\psi}\frac{\partial \phi_{sp,\psi}}{\partial z}\right) = R_v \tag{4}$$

$$J_\psi^n = i_0^n\times\left(exp\left(\frac{0.5F}{RT}\eta_\psi^n\right) - exp\left(\frac{-0.5F}{RT}\eta_\psi^n\right)\right) \tag{5a}$$

$$i_0^n = k_\psi^n\left(c_{p,\psi}^{n,max} - c_{p,\psi}^{n,surf}\right)^{1/2}\left(c_{p,\psi}^{n,surf}\right)^{1/2}\left(\frac{c_{e,\psi}}{c_{e,ref}}\right)^{1/2} \tag{5b}$$

$$\eta_\psi^n \;=\; \phi_{sp,\psi} - \phi_{e,\psi} - U_\psi^n \tag{5c}$$

$$-D_{eff,a}\left.\frac{\partial c_{e,a}}{\partial z}\right|_{z=0} = 0 \tag{6a}$$

$$-D_{eff,c}\left.\frac{\partial c_{e,c}}{\partial z}\right|_{z=L_a+L_s+L_c} = 0 \tag{6b}$$

$$-D_{eff,a}\left.\frac{\partial c_{e,a}}{\partial z}\right|_{z=L_a^-} = -D_{eff,s}\left.\frac{\partial c_{e,s}}{\partial z}\right|_{z=L_a^+} \tag{6c}$$

$$-D_{eff,s}\left.\frac{\partial c_{e,s}}{\partial z}\right|_{z=(L_a+L_s)^-} = -D_{eff,c}\left.\frac{\partial c_{e,c}}{\partial z}\right|_{z=(L_a+L_s)^+} \tag{6d}$$

$$\left.i_{e,a}\right|_{z=0} = 0 \tag{7a}$$

$$\left.i_{e,c}\right|_{z=L_a+L_s+L_c} = 0 \tag{7b}$$

$$-D_{p,\psi}^{n}\frac{\partial c_{p,\psi}^{n}}{\partial r^{n}}|_{r^{n}=0}=0 \quad (8a)$$

$$-D_{p,\psi}^{n}\frac{\partial c_{p,\psi}^{n}}{\partial r^{n}}|_{r^{n}=R_{p,\psi}^{n}}=J_{\psi}^{n} \quad (8b)$$

$$-\sigma_{eff,c}\frac{\partial \phi_{sp,\psi}}{\partial z}\Big|_{z=L_a+L_s+L_c}=I_{app} \quad (9a)$$

$$-\sigma_{eff,a}\frac{\partial \phi_{sp,\psi}}{\partial z}\Big|_{z=L_a}=0 \quad (9b)$$

$$-\sigma_{eff,c}\frac{\partial \phi_{sp,\psi}}{\partial z}\Big|_{z=L_a+L_s}=0 \quad (9c)$$

$$\phi_{sp,a}\big|_{z=0}=0 \quad (10)$$

Table ST2. List and description of the variables and symbols used in the model equations

Symbol	Description
ψ	Subscript indicating the domain (a for anode, s for separator, and c for cathode)
p	Subscript indicating the active material
n	Superscript indicating the type of the active material ($n=1$ for graphite, $n=2$ for hard carbon in the Gr-50 anode)
z	Coordinate for the cell thickness, m
$c_{e,\psi}$	Electrolyte concentration, mol/m^3
ε_{ψ}	Electrolyte volume fraction (porosity)
$D_{eff,\psi}$	Effective electrolyte diffusivity, m^2/s
$t_{+,\psi}^{0}$	Transference number for the Li-ions in the electrolyte
$a_{p,\psi}^{n}$	Surface area of the active material per unit volume of the electrode. For spherical particles, it is equal to $3\frac{\varepsilon_{p,\psi}^{n}}{R_{p,\psi}^{n}}$, m^2/m^3
J_{ψ}^{n}	Electrochemical reaction flux at the electrolyte/active material interface, mol/m^{2}s
$i_{e,\psi}$	Electrolyte current density, A/m^2
F	Faraday's constant, C/mol
R_v	Total reaction current per unit electrode volume, A/m^3
$R_{p,\psi}^{n}$	Radius of the active material particles, m
$\varepsilon_{p,\psi}^{n}$	Volume fraction of the active material particles in the electrode
L_{ψ}	Thickness of the domain, m
$c_{p,\psi}^{n}$	Li concentration in the active material, mol/m^3
r^{n}	Radial coordinate defined within the spherical active material particles, m
$D_{p,\psi}^{n}$	Diffusion coefficient of Li inside the active material particles, m^2/s
$\kappa_{eff,\psi}$	Effective electrolyte conductivity in the domain, S/m
$\phi_{e,\psi}$	Electrostatic potential of the electrolyte, V
R	Universal gas constant, Jmol/K

T	Cell temperature, K
$\frac{\partial\, ln(f_{\pm,\psi})}{\partial\, ln(c_{e,\psi})}$	Dependence of the electrolyte activity coefficient on the electrolyte concentration
$\sigma_{eff,\psi}$	Effective electronic conductivity of the electrode, S/m
sp	Subscript indicating the solid phase, which includes the active material, the carbon additive, and the binder, inside an electrode
$\phi_{sp,\psi}$	Electrostatic potential of the solid phase, V
I_{app}	Applied current density, A/m^2
i_0^n	Exchange current density used in the Butler Volmer equation, A/m^2
η_ψ^n	Local overpotential in the electrode that drives the electrochemical reaction, V
U_ψ^n	Open circuit voltage (OCV), V
$c_{p,\psi}^{n,surf}$	Local Li concentration on the surface of the active material particles
$c_{p,\psi}^{n,max}$	Maximum Li concentration inside the active material particles

The above system of coupled partial differential equations was solved using COMSOL Multiphysics 5.4a. The one-dimensional domain was discretized using elements with max size of 1×10^{-7} m. The multifrontal massively parallel sparse direct solver (MUMPS)[6] and a Generalized Alpha solver for time-stepping with a relative tolerance of 1×10^{-6} were employed. The value of $c_{e,ref}$ was set to 1 mol/m^3.

Model Parameterization

All the parameter values used for the models are listed in Table ST3 along with their source and a comparison with the ranges, except for the cathode parameters, which can be found in our previous paper. [7] Note that the cathode parameters were set such that it does not limit the anode kinetics and thus the results in this work would not depend on them as long as this requirement is met. Some of the model parameters were gathered from the literature or obtained experimentally; the remaining parameters were determined by fitting in a similar fashion as described in our previous work.[7] The open circuit voltages (OCV) for the graphite and hard carbon anodes are shown in Figure S17. The intrinsic electrolyte properties that vary with the electrolyte concentration are obtained from Ref 8 and are shown in Figure S18.[8] The intrinsic diffusivities of Li inside graphite as a function of the Li site fraction is obtained from the Ref 9 and is shown in Figure S19.[9] More details about the parameter selection, OCV measurements, etc. can be found here.[7] The fitting was carried out by matching the simulated anode voltages (vs. Li/Li$^+$ reference) for the three anodes with the corresponding three-electrode measurements. The models for the non-hybrid graphite and hard carbon anodes were parameterized first. It is noted that the values of effective electrolyte diffusivity were verified to be within 10% of the experimental value for graphite and within a factor of two for the hard carbon (Table ST1); as these are in agreement within the combination of experimental and modeling uncertainty, we retained the fit value for the simulations.

For the Gr-50 model, all the material properties were set to the same values as determined from the non-hybrid anodes except for two parameters. One is the effective electrolyte diffusivity and conductivity, which depends on the anode microstructure. In addition, another

parameter that must account for the experimental uncertainty in the electrode loading. The loading depends on three factors: electrode thickness, active material volume fraction, and the maximum Li concentration, which is directly proportional to active material density. While in principle there are uncertainties in all of these factors, the simulation results are only sensitive to the loading. Hence, we chose to treat the maximum Li concentration in hard carbon as a fitting parameter to account for the uncertainty. The values obtained for the maximum Li concentration are fairly close to each other (only ~5% difference between the value used for the hard carbon anode and that used in the Gr-50 anode, as shown in Table ST3), which shows that the aforementioned approach is reasonable.

Table ST3. Parameter values used in the simulations, along with their sources and comparison with the ranges of values surveyed from the literature.

Parameters	Values	Units	Sources	Range of values in literature (if applicable)
Intrinsic material properties				
Diffusion coefficient of the electrolyte, D_L	(2.2×10^{-10} – 4.24×10^{-10}) (Fig. S18b)	m^2/s	Literature [8]	--
Ionic conductivity of the electrolyte, κ_L	(1×10^{-6} – 9.5×10^{-1}) (Fig. S18a)	S/m	Literature [8]	--
Transference number in the electrolyte, t_+^0	1.1×10^{-1} – 3.7×10^{-1} (Fig. S18c)	--	Literature [8]	--
Activity coefficient of the electrolyte, $\frac{\partial\, ln(f_\pm)}{\partial\, ln(c_L)}$	0 – 2.5 (Fig. S18d)	--	Literature [8]	--
Diffusion coefficient of Li inside graphite, D_{Gr}	(6.6×10^{-16} – 4.2×10^{-13}) (Fig. S19)	m^2/s	Literature [9]	1×10^{-15} – 1×10^{-9} m^2/s [10]
Diffusion coefficient of Li inside hard carbon, D_{HC}	3.9×10^{-14}	m^2/s	Literature [11]	
Electronic conductivity of NMC, σ_{NMC}	6.8×10^{1}	S/m	Literature [12]	--
Electronic conductivity of graphite, σ_{Gr}	1×10^{2}	S/m	Literature [13]	--
Electronic conductivity of hard carbon, σ_{HC}	1×10^{2}	S/m	Literature [11]	
Graphite Anode				
Thickness (L_a)	6.8×10^{-5}	m	Experiment	--
Particle radius $(R_{p,a}^1)$	4.06×10^{-6}	m	Experiment	--
Electrolyte volume fraction (ε_a)	3.132×10^{-1}	--	Experiment	--
Active material volume fraction $(\varepsilon_{p,a}^1)$	6.456×10^{-1}	--	Experiment	--
Reaction rate constant (k_a^1)	2.574×10^{-10}	m/s	Fitting	1.7×10^{-11} – 1.5×10^{-10} m/s [13–17]
Max Li concentration in graphite $(c_{p,a}^{1,max})$	2.95×10^{4}	mol/m^3	Fitting	3.054×10^{4} – 3.192×10^{4} mol/m^3 [14–17]

Initial Li concentration in graphite ($c_{p,a}^{1}\big\vert_{t=0}$)	2.95×10^{1}	mol/m^3	Fitting	--
Li diffusion coefficient in graphite ($D_{p,a}^{1}$)	$0.2055\times D_{Gr}$	m^2/s	Fitting	--
Effective Li diffusion coefficient in the electrolyte ($D_{eff,a}$)	$2.6\times10^{-2}\times D_{L}$	m^2/s	Fitting	--
Effective electrical conductivity ($\sigma_{eff,a}$)	$5.36\times10^{-2}\times\sigma_{Gr}$	S/m	Fitting	$1\times10^{1}-2.2\times10^{2}$ S/m [14,17,18]
Effective ionic conductivity of the electrolyte ($\kappa_{eff,a}$)	$2.6\times10^{-2}\times\kappa_{L}$	S/m	Fitting	--
Initial electrolyte salt concentration ($c_{e,a}\big\vert_{t=0}$)	1×10^{3}	mol/m^3	Experiment	--
Hard Carbon Anode				
Thickness (L_a)	1.04×10^{-4}	m	Experiment	--
Particle radius ($R_{p,a}^{1}$)	1.64×10^{-6}	m	Experiment	--
Electrolyte volume fraction (ε_a)	3.114×10^{-1}	--	Experiment	--
Active material volume fraction ($\varepsilon_{p,a}^{1}$)	6.353×10^{-1}	--	Experiment	--
Reaction rate constant (k_a^1)	2.244×10^{-10}	m/s	Fitting	
Max Li concentration in Hard Carbon ($c_{p,a}^{1,max}$)	1.6667×10^{4}	mol/m^3	Fitting	
Initial Li concentration in Hard Carbon ($c_{p,a}^{1}\big\vert_{t=0}$)	1.6667×10^{1}	mol/m^3	Fitting	--
Li diffusion coefficient in Hard Carbon ($D_{p,a}^{1}$)	$1\times D_{HC}$	m^2/s	Fitting	--
Effective Li diffusion coefficient in the electrolyte ($D_{eff,a}$)	$4.76\times10^{-2}\times D_{L}$	m^2/s	Fitting	--
Effective electrical conductivity ($\sigma_{eff,a}$)	$9.71\times10^{-2}\times\sigma_{HC}$	S/m	Fitting	$1\times10^{1}-2.2\times10^{2}$ S/m [14,17,18]
Effective ionic conductivity of the electrolyte ($\kappa_{eff,a}$)	$4.76\times10^{-2}\times\kappa_{L}$	S/m	Fitting	--
Initial electrolyte salt concentration ($c_{e,a}\big\vert_{t=0}$)	1×10^{3}	mol/m^3	Experiment	--
Gr-50 Anode				
Thickness (L_a)	8.3×10^{-5}	m	Experiment	--
Electrolyte volume fraction (ε_a)	3.169×10^{-1}	--	Experiment	--
Active material volume fraction- Graphite ($\varepsilon_{p,a}^{1}$)	2.631×10^{-1}	--	Experiment	--
Active material volume fraction- Hard Carbon ($\varepsilon_{p,a}^{2}$)	3.634×10^{-1}	--	Experiment	--

Max Li concentration in Hard Carbon $\left(c_{p,a}^{2,max}\right)$	1.75×10^{4}	mol/m^3	Fitting	
Initial Li concentration in graphite $\left(c_{p,a}^{1}\big\vert_{t=0}\right)$	2.95×10^{-2}	mol/m^3	Fitting	--
Initial Li concentration in Hard Carbon $\left(c_{p,a}^{2}\big\vert_{t=0}\right)$	1.75×10^{1}	mol/m^3	Fitting	--
Effective Li diffusion coefficient in the electrolyte $(D_{eff,a})$	$3.5\times10^{-2}\times D_L$	m^2/s	Fitting	--
Effective electrical conductivity $(\sigma_{eff,a})$	$6.92\times10^{-2}\times\sigma_{Gr}$	S/m	Fitting	
Effective ionic conductivity of the electrolyte $(\kappa_{eff,a})$	$3.5\times10^{-2}\times\kappa_L$	S/m	Fitting	--
Initial electrolyte salt concentration $\left(c_{e,a}\big\vert_{t=0}\right)$	1×10^{3}	mol/m^3	Experiment	--
Separator				
Thickness (L_s) – three-electrode cell	2.2×10^{-4}	m	Experiment	--
Thickness (L_s) – pouch cell	1.2×10^{-5}	m	Experiment	--
Volume fraction of electrolyte (ε_s) – three-electrode cell	7.1×10^{-1}	--	Experiment	--
Volume fraction of electrolyte (ε_s) – pouch cell	4.7×10^{-1}	--	Experiment	--
Effective Li diffusion coefficient in electrolyte $(D_{eff,s})$	$5\times10^{-1}\times D_L$	m^2/s	Fitting	--
Effective ionic conductivity of the electrolyte $(\kappa_{eff,s})$	$5\times10^{-1}\times\kappa_L$	S/m	Fitting	--
Initial electrolyte salt concentration $\left(c_{e,s}\big\vert_{t=0}\right)$	1×10^{3}	mol/m^3	Experiment	--
Other				
Temperature	2.98×10^{2}	K	Experiment	--
1C current density	2.326×10^{1}	A/m^2	Experiment	--

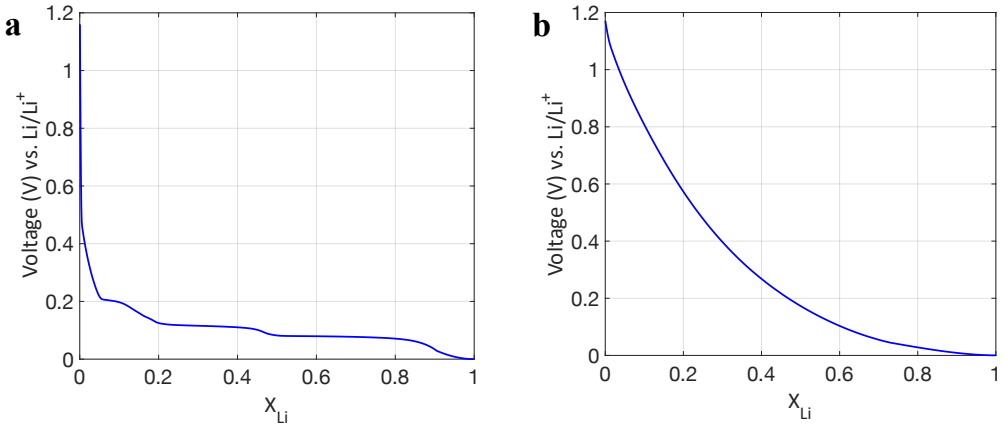

Figure S17. The open-circuit voltage as a function of the lithium site fraction for (a) graphite and (b) hard carbon as used in the simulations.

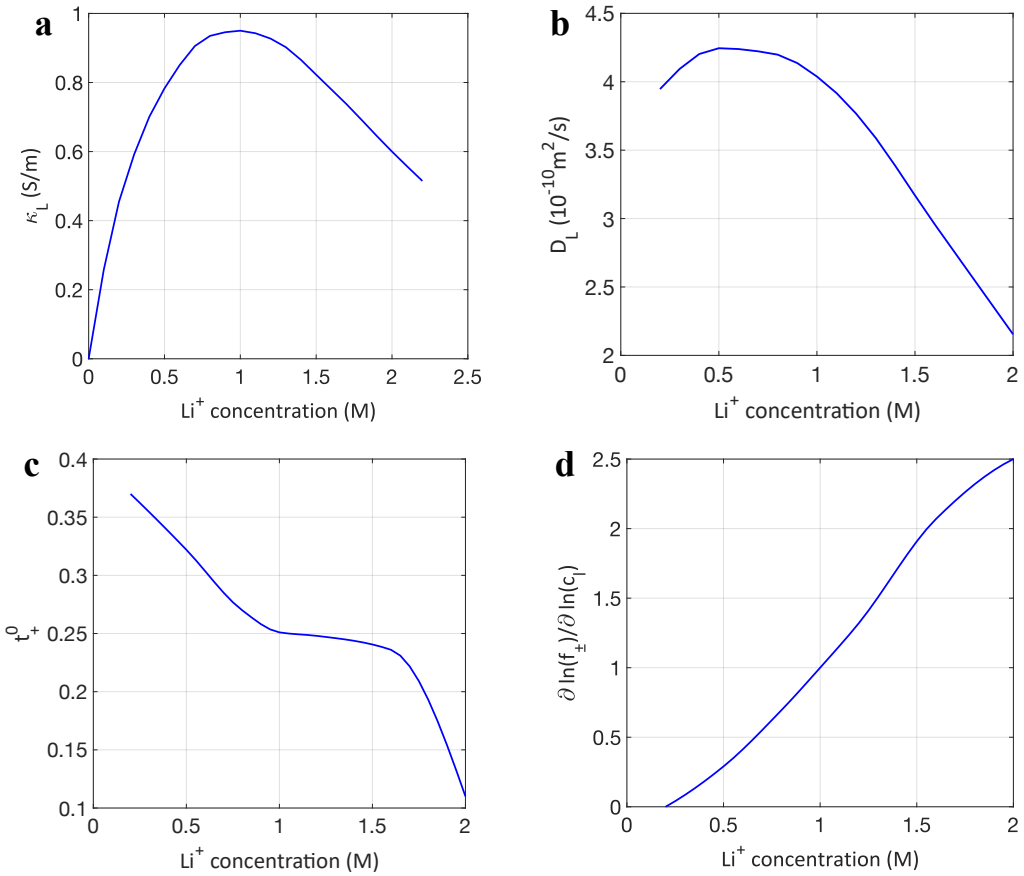

Figure S18. The intrinsic properties of the electrolyte as a function of Li-ion concentration. (a) Ionic conductivity, (b) diffusion coefficient, (c) transference number of Li-ion, and (d) the dependence of the salt activity coefficient on the electrolyte concentration.[8]

The comparison of the simulated and measured voltages for the three anodes at six different C-rates in the three-electrode cell configuration is provided in Figure S20. It should be noted that change in the reference voltage due to the change in the electrolyte concentration in the separator during charging was less than 10 mV at all times. Hence, we simply report the anode voltage with an assumed reference value of 0V at the middle of the separator. The match for the graphite (Figure S20a) and hard carbon (Figure S20b) are excellent at all the C-rates. The minor discrepancy between the experimental measurement and the simulated result for the graphite anode at 0.5C can be attributed to the uncertainty in the measurement. The match for the Gr-50 anode (Figure S20c) is good as well. The deviations at 4C and 6C can be attributed to the assumptions of the single-particle size instead of a distribution, and the isotropic solid-state diffusion in the model. Nonetheless, the results are expected to be robust,

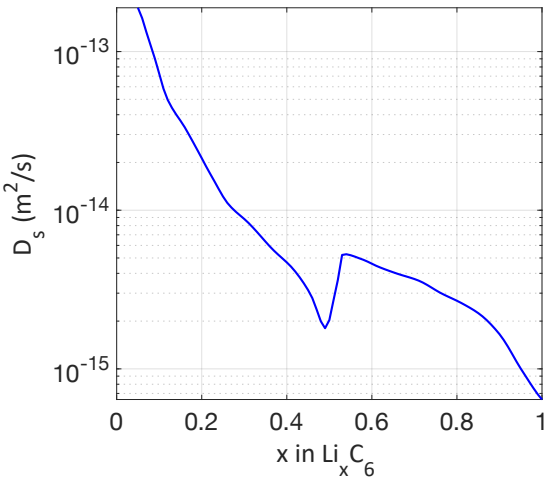

Figure S19. Li diffusion coefficient in graphite as a function of the Li site fraction.[9]

as the model reasonably reproduces the experimentally measured voltages for the Gr-50 anode for the same set of parameters as determined from the individual matches.

The parameterized models were then used to simulate the electrochemical performance of the graphite, hard carbon, and Gr-50 anodes at 4C and 6C in the pouch cell configuration. It should be noted that the pouch cell configuration has a thinner separator as compared to the three-electrode cell configuration (12 µm vs. 220 µm, as listed in Table ST3).

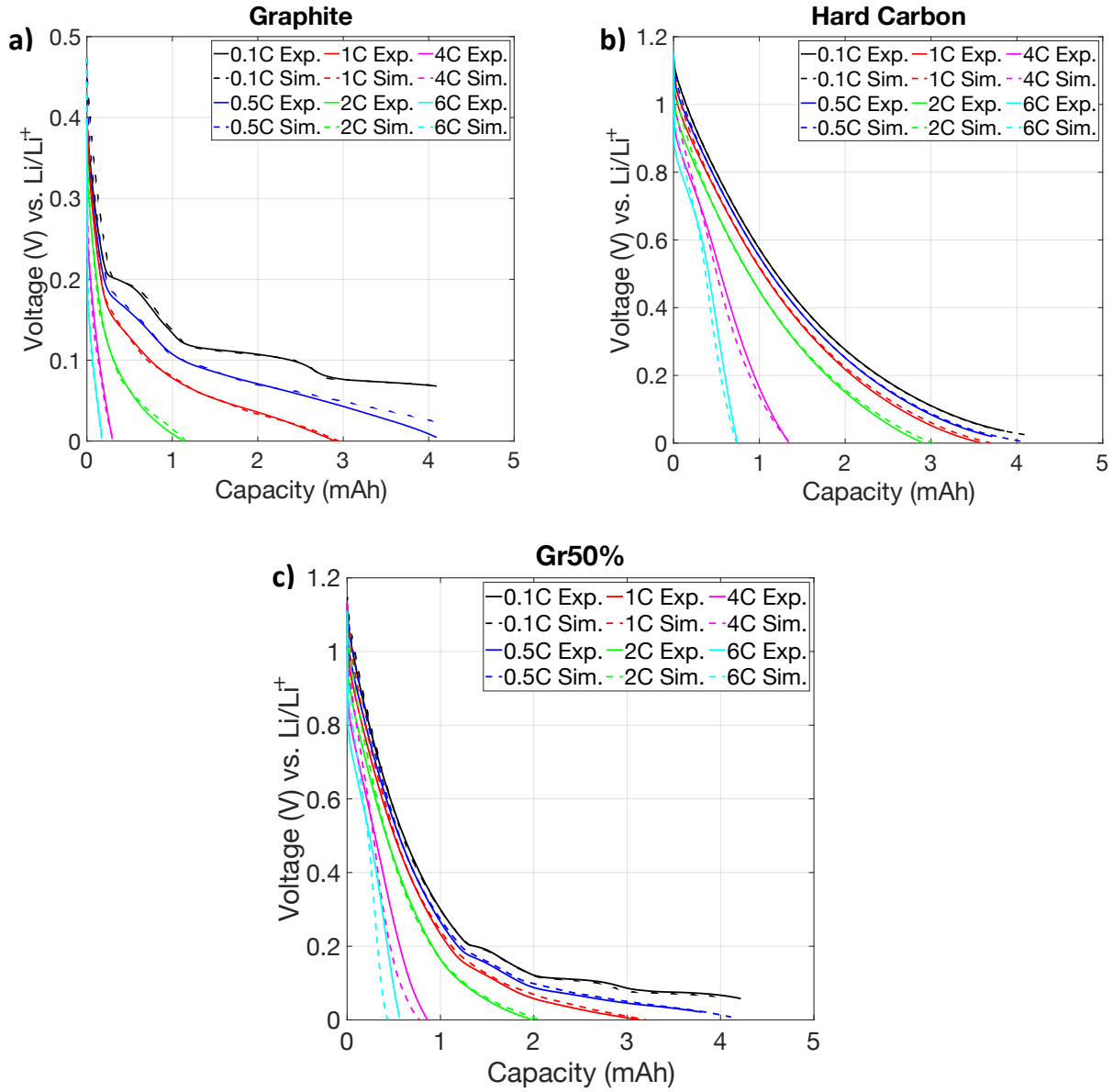

Figure S20. The comparison of the experimental and simulated voltages at six different C-rates for the (a) graphite, (b) hard carbon, and (c) Gr-50 anodes in the three-electrode cell configuration.

Figure S21 shows the fraction of the current contributed by each component in the Gr-50 anode during 4C charging in the pouch cell configuration. The blue and magenta curves represent the contributions by the graphite and hard carbon components, respectively. It can be seen that the sum of the current contribution by the two components is always equal to

one, as shown by the black curve. Moreover, three regimes are observed in the plot. The first regime is observed between 0 and 80 seconds, where the hard carbon component contributes most of the current as the graphite component is electrochemically inactive in the voltage range corresponding to that time period, except for the region near the anode/separator interface.

The second regime is observed between 80 and 290 seconds, where the contributions by the graphite and the hard carbon components monotonically increase and decrease, respectively. The last regime is observed from 290 seconds to the end of charging, where the current contributions remain nearly constant. Throughout the charging, the hard carbon component contributes to most of the current. This reduces the load experienced by the graphite component.

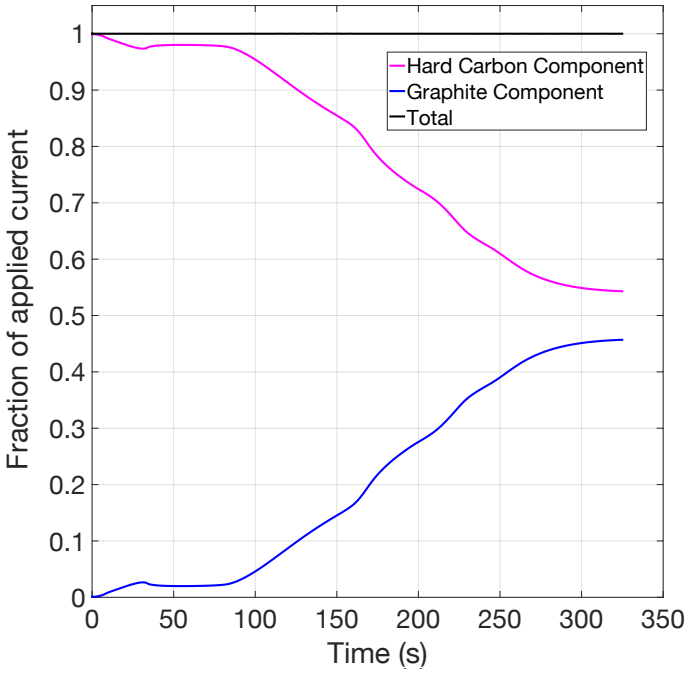

Figure S21. Fraction of the applied current contributed by the hard carbon (magenta) and the graphite (blue) components in the Gr-50 anode during 4C charging. The black curve represents the summation of the two components.

Figure S22 shows the comparison of H_{90} for the three anodes during 4C charging. As mentioned in the main text, the graphite anode progressively develops reaction inhomogeneity, with H_{90} rapidly decreasing from 0.86 to 0.61. In contrast, the hard carbon anode has a higher reaction homogeneity as the H_{90} value for it remains above 0.77 throughout charging. The H_{90} behavior for the Gr-50 anode is more complex, as there is a rapid decrease in the H_{90} value followed by a plateau and an increase. The non-monotonic behavior is under investigation at the time of writing and will be explained in detail in a future study. Nonetheless, it can be seen that H_{90} for Gr-50 is always higher than that for the graphite anode throughout charging. The low H_{90} value at the very beginning of charging in all the three anodes is because of the lower ionic conductivity as compared to the electronic conductivity, due to which the reaction current density is initially

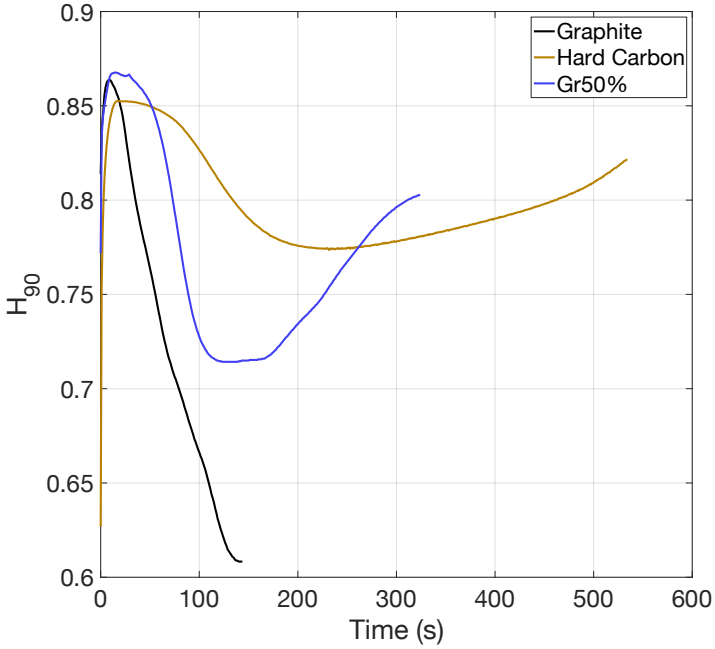

Figure S22. Comparison of H_{90} for the graphite (blue), hard carbon (magenta), and Gr-50 (black) anodes for 4C charging.

high near the anode/separator interface, as discussed in Ref 19.[19]

Figure S23 shows the results for the 6C galvanostatic charging of the three anodes in the pouch cell configuration. The simulations were terminated when the anode voltage (vs. Li metal reference) reached 0 V, as in the 4C simulations. The trends observed in the simulated voltage and the reaction current density distribution for the 6C simulations for the three anodes are similar to the trends observed in the 4C results. Therefore, our discussion in the main text also applies here. In summary, the graphite anode has a highly inhomogeneous reaction current density distribution, which makes it susceptible to Li plating. This inhomogeneity can be reduced by blending the graphite anode with hard carbon, which reduces the load on the graphite particles.

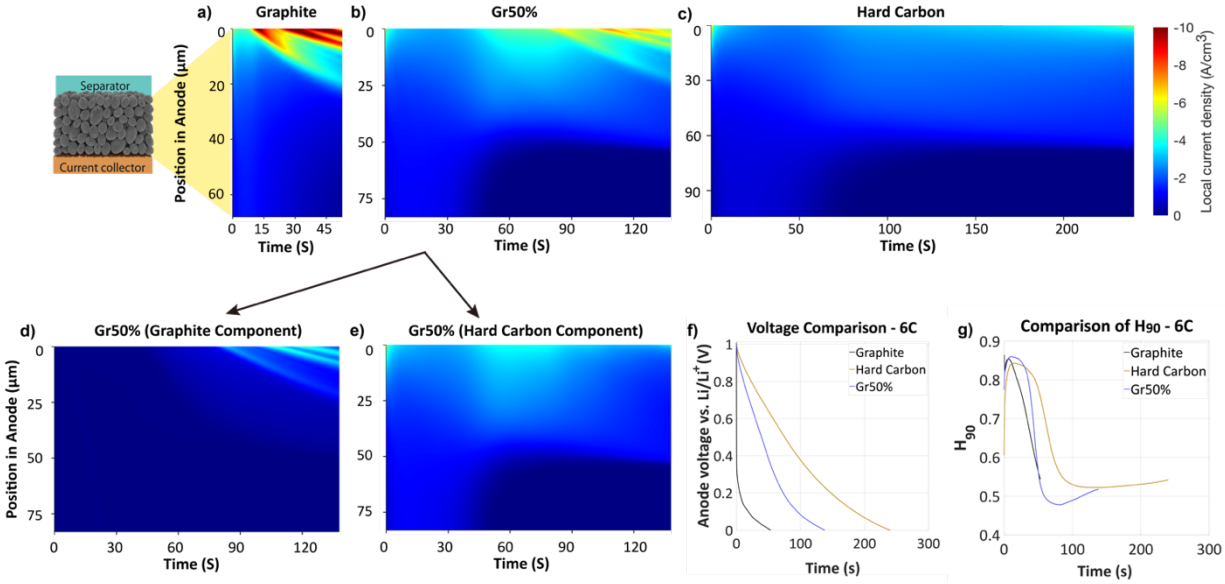

Figure S23. Evolution of the local reaction current density as a function of the position along the thickness of the a) graphite, b) Gr-50, and c) hard carbon anodes during 6C charging. The schematic on the left of a) shows the orientation of the anodes in the evolution plots. The top edge and the bottom edge of each evolution plot correspond to the anode/separator and anode/current collector interfaces, respectively. (d-e) Evolution of the local current density contribution by the graphite and hard carbon components in Gr-50. The maximum magnitude on the color bar has been limited to 10 A/cm^3 to enable a better comparison among the three anodes, although the maximum magnitude of the current density observed in the graphite anode is ~13 A/cm^3. Therefore, the dark red regions in the graphite plot have values between -10 A/cm^3 and -13 A/cm^3. (f) Comparison of the simulated voltage vs. time plots obtained for 6C charging for the three anodes. (g) Comparison of H_{90} for the three anodes.

Experimental section

Electrode fabrication

Electrodes were prepared using a pilot-scale roll-to-roll processing facility at the University of Michigan Battery Lab. Battery-grade graphite (Superior Graphite) and hard carbon (Pred Materials International) were used as the active anode materials. Active materials were first mixed with CMC/SBR binder in a weight ratio of 94/3/3 in deionized water to make a homogeneous slurry. The resulting anode slurry was then casted onto 10 μm copper foils (Fukuda). The specific capacity of the graphite and hard carbon used in this work was measured (at a C/10 rate) to be 335 mAh/g and 275 mAh/g, respectively. Therefore, areal mass loadings were slightly adjusted for hybrid anodes with varying graphite/hard carbon blend ratio to obtain the same areal capacity loading of ~3 mAh/cm^2. After casting, the anodes were dried and calendered to a porosity of 31-33%. $LiNi_{0.5}Mn_{0.3}Co_{0.2}O_2$ (NMC-532, Toda America) was used as the cathode material. The cathode formulation was 92 wt.% NMC-532, 4 wt.% C65 conductive additive, and 4 wt.% PVDF binder. The cathode slurry was casted onto 15 μm aluminum foils (Targray) with a total areal mass loading of 16.58 mg/cm^2 and calendered to a porosity of 34%.

Pouch cell assembly

Fabricated electrodes were first baked in vacuum ovens at 90^{o}C overnight to remove any residual moisture prior to pouch cell assembly. Pouch cells were assembled in a dry room (< -50 ^{o}C dew point) at the University of Michigan Battery Lab. Each pouch cell was constructed of 4/5 cathode/anode double-sided electrodes with 12 μm polyethylene separators (ENTEK). A N/P ratio of 1.16 was fixed for all five types of cells. The electrode area was ~70 cm^2 on each side. 1M $LiPF_6$ in 3/7 EC/EMC with 2% VC additive (SoulBrain MI) was used as the electrolyte. After electrolyte filling, cells were vacuum sealed and allowed to rest for 12 hours to ensure full electrolyte infiltration into the electrodes. Subsequently, formation cycles were performed at C/10 rate between 2.7-4.2 voltage window. Afterwards, the cells were transferred back into the dry room, degassed to release gases produced during the formation, and then re-sealed.

Pouch cell testing

Pouch cells were cycled in a temperature-controlled chamber at 30 ^{o}C using a Maccor 4000 series automated test system. To evaluate the fast-charge capability of the hybrid anodes, a CC-CV charging protocol with a charging time cutoff was used (15 min for 4C and 10 min for 6C). For 4C (15-min) fast charging, pouch cells were first charged at a constant current (CC) of 4C rate until reaching an upper voltage cutoff of 4.2V, and then charged at constant voltage (CV) until a total charging time (CC+CV) of 15 minutes was reached. For 6C (10-min) fast charging, the applied CC current was 6C rate and the total charging time was limited to 10 minutes. Throughout the course of cycling, the discharge rate was fixed at 1C with a voltage cutoff of 2.7 V without any CV hold.

It is noted that due to the varying ICE values, the hybrid pouch cells have different cell capacities after formation cycles (Figure 3d). This can make the rate performance comparison difficult since the applied current (in C-rate) is proportional to the cell capacity. To facilitate a more direct comparison between all 5 types of pouch cells, here we define the applied current solely based on the capacity of the graphite cell after formation (1.3 Ah). In other words, during 4C and 6C fast charging, a current of 5.2 A and 7.8 A was applied on all pouch cells. We believe that this is a valid comparison since all the anodes have the same areal capacity loading

(3 mAh/cm^2). Therefore, the applied current density is the same with respect to the anodes during fast charging.

Three-electrode electrochemical measurements

Three-electrode measurements were performed using a commercial electrochemical test cell (ECC-PAT-Core, EL-CELL). In this setup, the hybrid anodes were used as the working electrode and Li metal was used as the counter electrode. In addition, a ring-shaped Li metal was used a reference electrode to measure the potential of the hybrid anodes with respect to Li/Li$^+$. Electrochemical data was collected using a BioLogic VSP potentiostat (Bio-Logic USA), which can measure the potential of the working and counter electrodes vs. the reference electrode potential.

Materials characterization

Post-mortem SEM analysis was performed to characterize Li plating during fast-charge cycling. Cycled pouch cells were first fully discharged to 2.7V and then transferred into an argon-filled glovebox (MBRAUN). Electrodes were carefully collected from the pouches and rinsed thoroughly with dimethyl carbonate (DMC) several times to remove any electrolyte residues. The cleaned electrodes were subsequently dried and stored in the glovebox antechamber under vacuum before transferred into SEM for imaging. SEM analysis was performed using a Tescan MIRA3 FEG SEM at the Michigan Center for Materials Characterization.

Tomography image analysis

Tomography

X-Ray tomography images were obtained at the TOMCAT beamline at the Paul Scherrer Institute (PSI). Samples were prepared by punching cylindrical pieces of 1 mm diameter out of the electrodes and then attaching to the sample holder with a 0.5 mm thick disk of epoxy (Bühler) between the sample holder and the actual sample.

The beamline was operated using a parallel beam with a beam energy of 20 keV and a ring current of 400 mA. The images were obtained using a CCD camera (PCO.Edge 5.5) with a microscope (Opt.Peter MB op) with a magnification of 40 and an exposure time of 300 ms per projection. A total of 1501 projection per sample consisting of 2560 voxels in x- and y-direction and 1162 voxels in z-direction with a voxel size of 162.5 nm were collected. 10 darks and 100 flats were taken to measure beam parameters and background noise. 3-D images were obtained by rotating the sample by 180° in 0.12° steps around the z-axis. 3-D image reconstruction was done by using the Paganin algorithm[20] with delta = 10^{-9}, beta = 10^{-10}, distance = 5 mm, and pixel size = 162.5 nm.

Image stack processing using ImageJ

The image stack of each electrode was processed using ImageJ to decrease the image stack size by cutting the electrode surroundings and correcting for tilts in the x- or y-direction. ImageJ was also used for image overlays to compare filtered data to pristine data and segmented data to pristine data.

Segmentation using MATLAB

Image segmentation was performed by iterative greyscale thresholding and morphological operations. A threshold correction of ±0.05 with respect to the value from the Otsu threshold method is chosen to identify (a) the solid phase (Otsu + 0.05) -1 and (b) the pore space 0-

(Otsu – 0.05) with high confidence according to their grey-values (Figure S24). The electrode regions with intermediate grey values of Otsu ± 0.05 were iteratively assigned to the solid phase and pore space with morphological operations. Specifically, 5% of the voxels of the intermediate grey values were changed to white solid phase seeds that were randomly placed in this spatial region and iteratively dilated with cubes of 2-voxel-size edge length. The process also ensured that the dilation did not extend the newly created region into the previously assigned solid or pore space regions.

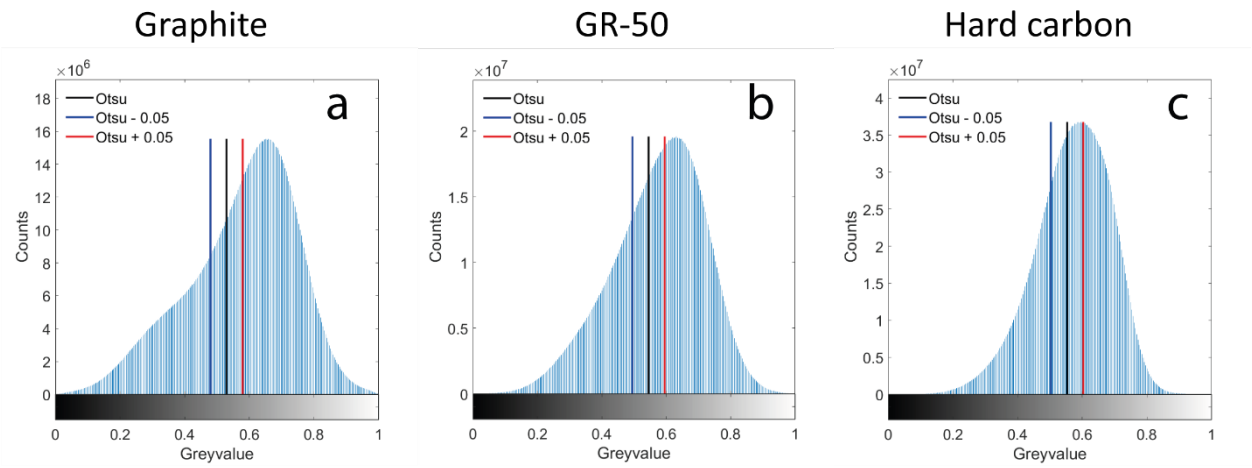

Figure S24. Grey-value histograms of the (a) graphite, (b) Gr-50, and (c) hard carbon electrodes. The calculated Otsu threshold (black line) and its correction by -0.05 (blue line) and +0.05 (red line) are shown in the figures.

Representative volume element

To analyze the electrode properties and acquire statistical information, a cubic sub-volume with an edge-length of 346 voxels (56.23 µm) was used. The sub-volume size was kept the same for all three electrodes to ensure no difference could originate from a change in the sub-volume size.[21] An analysis using a 1000 x 1000 x 346 voxel (162.5 µm x 162.5 µm x 56.23 µm) volume was performed (shown below). The acquired values for average porosity and pore size are similar between the 346 x 346 x 346 voxel and 1000 x 1000 x 346 voxel sample sizes, indicating that the chosen sub-volume size (346 x 346 x 346 voxel) is representative.

Size	Average porosity [%]	Average Pore size [µm]
346 x 346 x 346	32.3	1.02
1000 x 1000 x 346	32.6	1.01

References

[1] F. Meyer, *Signal Processing* **1994**, DOI 10.1016/0165-1684(94)90060-4.

[2] N. Ogihara, S. Kawauchi, C. Okuda, Y. Itou, Y. Takeuchi, Y. Ukyo, *J. Electrochem. Soc.* **2012**, *159*, A1034.

[3] N. Ogihara, Y. Itou, T. Sasaki, Y. Takeuchi, *J. Phys. Chem. C* **2015**, *119*, 4612.

[4] J. Landesfeind, J. Hattendorff, A. Ehrl, W. A. Wall, H. A. Gasteiger, *J. Electrochem. Soc.* **2016**, *163*, A1373.

[5] M. Doyle, J. Newman, *J. Electrochem. Soc.* **1996**, *143*, 1890.

[6] P. R. Amestoy, I. S. Duff, J.-Y. L'Excellent, *Comput. Methods Appl. Mech. Eng.* **2000**, *184*, 501.

[7] K. Chen, M. J. Namkoong, V. Goel, C. Yang, S. Kazemiabnavi, S. M. Mortuza, E. Kazyak, J. Mazumder, K. Thornton, J. Sakamoto, N. P. Dasgupta, *J. Power Sources* **2020**, *471*, 228475.

[8] A. Nyman, M. Behm, G. Lindbergh, *Electrochim. Acta* **2008**, *53*, 6356.

[9] M. D. Levi, D. Aurbach, *J. Phys. Chem. B* **1997**, *101*, 4641.

[10] M. Ender, *J. Power Sources* **2015**, *282*, 572.

[11] T. S. Dao, C. P. Vyasarayani, J. McPhee, *J. Power Sources* **2012**, *198*, 329.

[12] M. Ecker, S. Käbitz, I. Laresgoiti, D. U. Sauer, *J. Electrochem. Soc.* **2015**, *162*, A1849.

[13] Z. Du, D. L. Wood, C. Daniel, S. Kalnaus, J. Li, *J. Appl. Electrochem.* **2017**, *47*, 405.

[14] D. Sauerteig, N. Hanselmann, A. Arzberger, H. Reinshagen, S. Ivanov, A. Bund, *J. Power Sources* **2018**, *378*, 235.

[15] M. Ecker, T. K. D. Tran, P. Dechent, S. Käbitz, A. Warnecke, D. U. Sauera, *J. Electrochem. Soc.* **2015**, *162*, A1836.

[16] M. Tang, P. Albertus, J. Newman, *J. Electrochem. Soc.* **2009**, *156*, 390.

[17] J. Schmalstieg, C. Rahe, M. Ecker, D. U. Sauer, *J. Electrochem. Soc.* **2018**, *165*, A3799.

[18] K. A. Smith, C. D. Rahn, C. Y. Wang, *Energy Convers. Manag.* **2007**, *48*, 2565.

[19] J. S. Newman, C. W. Tobias, *J. Electrochem. Soc.* **1962**, *109*, 1183.

[20] T. . Gureyev, A. Pogany, D. . Paganin, S. . Wilkins, *Opt. Commun.* **2004**, *231*, 53.

[21] S. Müller, J. Eller, M. Ebner, C. Burns, J. Dahn, V. Wood, *J. Electrochem. Soc.* **2018**, *165*, A339.